REVIEW OF X-33 HYPERSONIC AERODYNAMIC AND AEROTHERMODYNAMIC DEVELOPMENT

Richard A. Thompson
NASA Langley Research Center

Abstract

A review of the experimental and computational studies performed at NASA Langley Research Center (LaRC) to support the optimization and benchmarking of the hypersonic aerodynamic and aerothermodynamic databases for the X-33 vehicle is presented. A synoptic of the testing, computational, and analysis capabilities at LaRC applied to these studies is given. Analyses of the hypersonic aerodynamic characteristics, control surface effectiveness, and reaction control system effects are discussed. Experimental measurement of the aerodynamic heating via the global thermographic phosphor technique and development of a hypersonic boundary-layer transition correlation for X-33 is described. Computational results used to complement the experimental program and to assess the vehicle aerodynamic and aerothermodynamic characteristics in flight are presented. The technical findings, impacts, and lessons learned from the studies are discussed.

1 Overview of the X-33 Program

1.1 Background

In 1993, an internal NASA study [1] proposed development of a fully reusable, rocket powered, single-stage-to-orbit (SSTO) vehicle capable of delivering 25,000 lbs (including crew members) to the International Space Station. This new launch system would combine efficient operations with increased safety and provide access to space at greatly reduced cost. The "Access-to-Space" study identified critical technologies that required development before a SSTO reusable launch vehicle (RLV) could be successfully flown. NASA also recommended that this new system be commercially owned and operated, unlike previous programs. There-fore, an approach was followed whereby NASA would work cooperatively with an industry partner to mature the technology for RLV through development of a sub-scale technology demonstration, i.e. the X-33 program.

The X-33 program was organized as an industry-led partnership with NASA in which the companies negotiated development tasks with the various NASA centers prior to submitting proposals. Industry would utilize government facilities and share in the program costs. A Phase I competition for X-33 was held in 1995 among the industry leaders (Lockheed-Martin, Rockwell, McDonnell Douglas/Boeing). Lockheed-Martin Skunk Works (LMSW) was ultimately awarded the program to continue into Phase II and toward construction and flight of the X-33 vehicle. The X-33 program (Phase I and Phase II) had ambitious, fast-paced schedules with a total time from development to flight of 3-4 years. Development of VentureStar , the full-scale operational RLV, progressed in parallel with the X-33 program [2].

Figure 1. The Lockheed-Martin X-33 and early RLV compared to Shuttle.

1.2 Configuration

The Lockheed-Martin concept for X-33 (and RLV) follows a long history of lifting-body development [3] in the United States. On X-33, canted fins, twin vertical tails, and dual body flaps are incorporated for aerodynamic control of the lifting body. The vehicle is powered by two linear aerospike engines mounted on the base. A rendering of X-33 relative to the Space Shuttle and an early RLV concept is presented in Figure 1 while the drawings illustrated in Figure 2 show more details and give the primary dimensions of the vehicle.
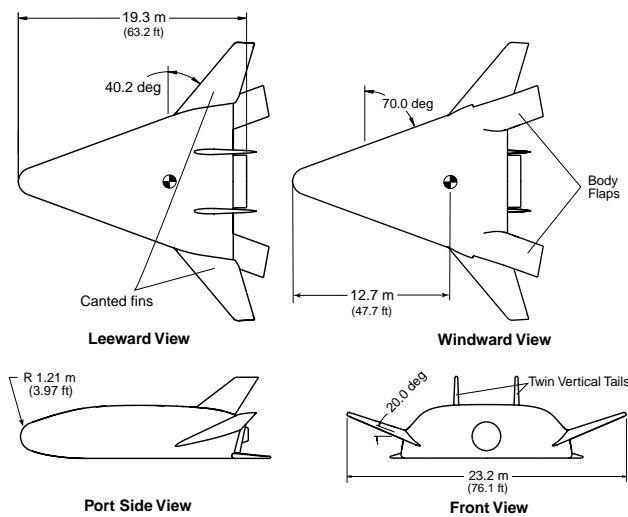

Figure 2. Primary geometric features of the Lockheed-Martin X-33 vehicle (from Hollis, et al. [4]).

A unique feature of the X-33 is the use of metallic panels for the windward surface thermal protection system (TPS). These TPS panels vary in size depending on body location and are arranged in a herringbone pattern with overlapping edges to eliminate gaps and fillers. A sketch of the panels on the windward surface along with the TPS materials employed over the remaining vehicle is given in Figure 3. The metallic panels are expected to provide benefits in vehicle operability relative to a ceramic TPS such as employed on the Shuttle Orbiter.
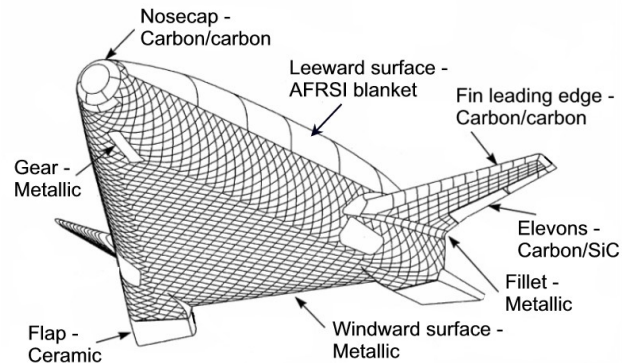

Figure 3. TPS material layout.

1.3 Flight

The X-33 was designed as a sub-orbital vehicle with two basic flight trajectories from its launch site at Edwards Air Force Base (AFB), California. The first is a high performance trajectory that would reach 250,000 ft at Mach 15 and land at Malmstrom AFB, Montanna. The second is a lower Mach 10 flight reaching 180,000 ft to Michaels AFB, Utah. Design of the X-33 thermal protection system was based on the Malmstrom trajectory but the first flights will be along the more benign path to Michaels. During descent, the vehicle attitude is maintained between 30 and 40-deg until approximately Mach 5. Figure 4 depicts the descent portion of the two trajectories and shows the operating envelopes of the ground-based facilities used in the work reviewed herein.
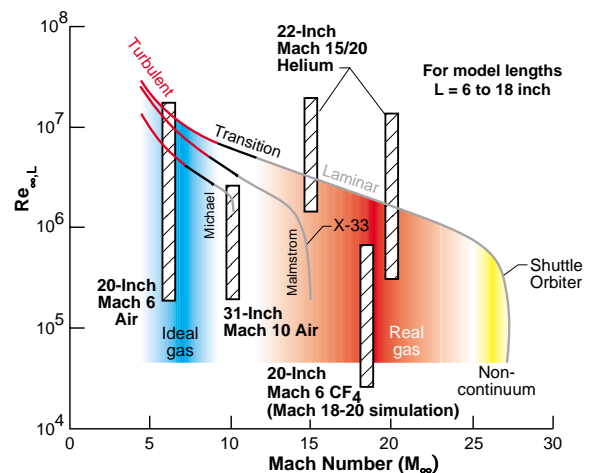

Figure 4. Mach number – Reynolds number simulation capability (adapted from Miller [5]).

The sub-orbital flight demonstrations of X-33 will test most flight and operational aspects of the future RLV; however, it should be noted the flights will not provide aerothermodynamic information about the low density, hypervelocity flight encountered during reentry from low earth orbit (LEO).

1.4 Role in X-33 Program

The Aerothermodynamics Branch (AB) at NASA Langley Research Center (LaRC) has played major roles in Phase I and Phase II of the X-33 program. During the 1995 Phase I study, the AB simultaneously supported the screening, design, and optimization of three industry concepts over a 12-month period. During Phase II, formal Task Agreements with LMSW were established whereby the AB would support the development, final design, and benchmarking of Lockheed's lifting body concept. This commitment posed a significant challenge to the AB since resources were shared with several competing programs (e.g. X-34, X-38, and X-43). Miller [6,5] gives a general review of the programmatic difficulties and the lessons learned from the AB's effort during this period of intense work.

The purpose of the present paper is to provide a technical review of several major aerodynamic and aerothermodynamic studies performed by the AB in support of the X-33 development. As such, this report presents the perspective of NASA LaRC, and the Aerothermodynamics Branch in particular. The technical findings, impact, and lessons learned from development of the aerodynamic and aerothermodynamic databases for the X-33 vehicle are presented. A typical design process supported by the AB begins with the screening of initial concepts and follows through optimization of the vehicle shape and then into benchmarking of the final design as depicted in Figure 5. Data from these studies form the basis for vehicle design and flight and provide critical inputs to other major systems (e.g. guidance and control, TPS design, structural loads). A final, but often-unrealized step, is the validation of design tools with flight-derived data as shown in the figure.
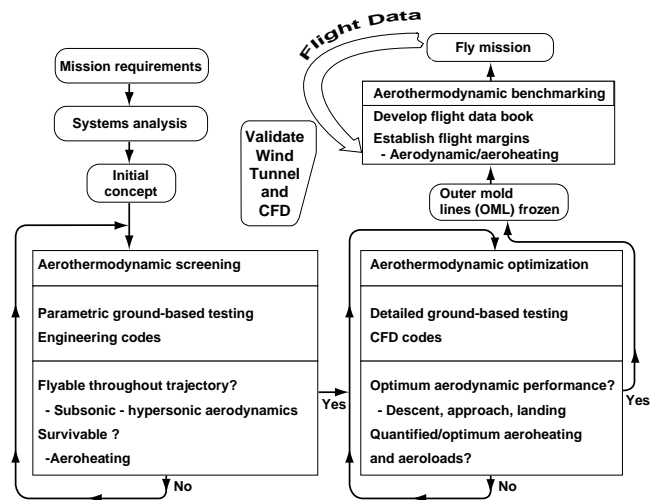

Figure 5. Aerothermodynamic process (adapted from Miller [5]).

The next section of this paper describes the experimental and computational capabilities at LaRC that were used to support the design process for X-33. The remaining sections present selected results that highlight the technical contributions. The paper focuses first on hypersonic aerodynamic testing (primarily, pitch control issues) and assessment of the reaction control system (RCS), followed by assessment of global and local aerodynamic heating, including a discussion of the hypersonic boundary-layer transition correlations that were developed.

2 Experimental Facilities and Testing

2.1 Aerothermodynamic Facilities Complex

The experiments reviewed in this paper were conducted in four facilities of the Aerothermodynamic Facilities Complex at NASA Langley Research Center: the 20-Inch Mach 6 Air Tunnel, the 31-Inch Mach 10 Air Tunnel, the 20-Inch Mach 6 CF_4 Tunnel, and the 22-Inch Mach 20 Helium Tunnel. Table 1 gives a summary of the nominal reservoir and corresponding free-stream flow conditions in each facility along with the Reynolds number range available. A detailed description of these facilities along with their performance characteristics, history, and capabilities is given by Micol [7].

Table 1. Nominal flow conditions.

Facility	P_t, psi	T_t, °R	M_∞	q_∞, psi	$Re_\infty \times 10^{-6}$, ft^{-1}		γ_∞
					Nominal	Range	
20-Inch Mach 6 Air	125	910	6	2.0	2.0	0.5 to 8	1.4
31-Inch Mach 10 Air	1450	1800	10	2.2	2.2	0.5 to 2.1	1.4
20-Inch Mach 6 CF$_4$	950	1150	6	0.9	0.4	0.05 to 0.7	1.15
22-Inch Mach 20 He	1000	530	20	1.7	7.5	2.4 to 22	1.67

2.2 Aerodynamic Testing

All of the hypersonic X-33 aerodynamic tests were performed with a 0.007-scale stainless steel model designed and fabricated at LaRC. The model included removable canted fins, body flaps, vertical tails, and engine nozzle components. The removable components were interchangeable with deflected control-surface parts or with off-blocks that were machined to the fuselage contour. The model off-blocks enabled configuration buildup tests to investigate the aerodynamics of the baseline vehicle (all components installed; all deflections zero) and all combinations of the fuselage, control surfaces, and engine nozzle.

The six force and moment components on the vehicle were measured on a top-mounted blade strut for angles of attack (α) over 25 deg to minimize support interference effects. A straight sting was employed at lower angles of attack with a 10 deg overlap between the two mounting systems to insure continuity of the data. An experimental uncertainty was assigned to all data based on a measured ±0.5% uncertainty in the balance at full-scale load.

2.3 Aerothermodynamic Testing

Measurements to determine aerodynamic heating were performed using a two-color relative-intensity phosphor thermography technique [8-10] to enable nonintrusive optical acquisition of the test data. With this technique, silica ceramic wind-tunnel models are slip casted [11] and coated with a mixture of phosphors that fluoresce in two regions of the visible spectrum (red and green) when illuminated with ultraviolet light. The fluorescence intensity is dependent on the amount of incident light and local temperature of the phosphors. By acquiring fluorescence intensity images of an illuminated model exposed to the wind-tunnel flow, surface temperature can be inferred for portions of the model in the camera's view. A temperature calibration of the system conducted prior to the test provides the data needed to convert the two-color images to quantitative values of surface temperature. Acquiring video images (temperatures) at 30 frames/sec during the wind-tunnel run enables a corresponding global heat-transfer distribution to be computed. Comparisons of heat transfer measurements using conventional thin-film resistance gauges and the thermographic phosphor technique have shown [10] excellent agreement. Accuracy of the phosphor system and data reduction is ±8% and the overall accuracy on heating rate is ±15% due to all factors [10].

This technique, which has been widely used at LaRC, offers several advantages over conventional test methods. Foremost, the measurements provide a quantitative resolution of global temperatures and heating unlike discrete gauge measurements. In addition, the model construction, testing, and data reduction can be performed significantly faster and cheaper than other techniques allow. The global resolution and rapid testing this method allows were particularly important for the X-33 work in order to study transition fronts on a complex three-dimensional vehicle in a timely and efficient manner. Over 70 ceramic models were constructed to support aerothermodynamic testing of the X-33 vehicle. Advances were made in fabrication techniques of the ceramic models in response to program requirements (e.g. models with highly a detailed surface to simulate bowing of individual TPS panels).

3   Computational Methods

3.1 Engineering Code

Computation of surface heating, surface streamlines, and boundary layer parameters was performed using the LATCH (Langley Approximate Three-Dimensional Convective Heating) code [12]. LATCH is based on the axisymmetric analog and uses approximate integral methods for general three-dimensional boundary layer results. The code is coupled with inviscid (Euler) solutions to provide the boundary layer edge conditions. LATCH employs an engineering technique [13] to calculate heating on three-dimensional hypersonic vehicles and has been shown [12] to be in good agreement with both experimental and Navier-Stokes results.

3.2 Euler Code

The FELISA code [14,15] combines a series of programs that generate unstructured tetrahedral grids over three-dimensional vehicles and solve the steady Euler equations. This proves to be an invaluable combination since it enables very rapid modeling and solutions for complex configurations. Algorithms exist in FELISA to solve flows ranging from transonic to hypersonic speeds with gas chemistry models for air (perfect gas and equilibrium), CF_4, and the Mars atmosphere (CO_2).

3.3 Navier-Stokes Codes

Two Navier-Stokes codes were routinely applied in work reviewed herein. The LAURA (Langley Aerothermodynamic Upwind Relaxation Algorithm) code [16] uses a finite-volume shock-capturing approach to solve high-speed ($M_\infty > 3$) steady viscous and inviscid flow problems. The algorithm incorporates a point-implicit relaxation scheme to obtain solutions efficiently on multi-processor and massively parallel computers. The code has been successfully applied to a full range of hypersonic vehicles and flight conditions during its evolution over the past decade. LAURA includes models for perfect gas, equilibrium air, and thermal and chemical nonequilibrium air in addition to mod-

els for CF_4 and a Mars atmosphere. A unique feature of the LAURA code is the ability to perform one-dimensional grid adaption in order to resolve high gradients in the boundary layer and across a bow shock.

Like LAURA, the GASP (General Aerodynamic Simulation Program) code [17] employs a finite-volume, shock-capturing approach to solve both inviscid and viscous flow fields on structured grids. GASP employs a wide range of algorithms and models to solve flows from subsonic through hypersonic conditions. Equivalent thermochemical models exist in the GASP code in comparison with LAURA. The methodology for one-dimensional grid adaption employed by LAURA has been incorporated into the GASP solution procedure.

3.4 Grid Topology and Generation

The complex geometry in the base region of X-33 posed a challenge for grid generation and analysis with detailed CFD (Navier-Stokes and Euler). Consequently, two models of the base region emerged; the first attempted to capture the full geometric complexity of the vehicle and the second used an extended fuselage to simplify the problem. Figure 6 illustrates the fuselage extension that covered the base region and permitted solutions over the entire surface (including body flap and canted fin) without calculation of the complicated wake flow. A limited number of computations were performed without this fuselage extension but the majority of cases used the simplified geometry.
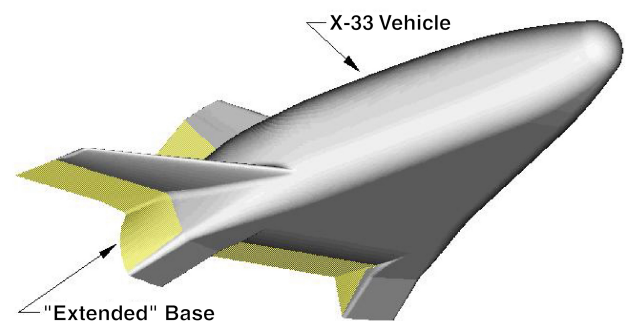

Figure 6. Computational surface model of X-33 geometry.

Structured grid generation has traditionally been a difficult and time-consuming process in the application of Navier-Stokes codes. However, the arduous requirements for grid generation on X-33 promoted improvements in the grid generation process; in particular, the capability to smooth and manipulate complex structured grids. Alter [18,19] refined the methodology and software that performed grid smoothing and manipulation into the VGM (Volume Grid Manipulator) code [20] during this period. The VGM code evolved from a simple grid conversion tool to a sophisticated scripting program that proved invaluable for grid quality improvements, grid repairs, and batch processing of grids among other features.

4   Contributions to the X-33 Program

4.1 Aerodynamics

Aerodynamic screening of the Lockheed X-33 configuration was completed and iterations to optimize the aerodynamic stability and control were initiated during the Phase I competition. Phase II work was mainly intended to generate the benchmark data to be included in the vehicle aerodynamic flight databook. The focus of this review concerns the testing performed in the LaRC hypersonic facilities during Phase II. These tests represented a major contribution to the overall experimental aerodynamic database achieved via tests at other Langley facilities (e.g. the Low Pressure Turbulence Tunnel (LTPT), the 14×22-Foot Wind Tunnel, the Unitary Plan Wind Tunnel (UPWT), and 16-Foot Transonic Tunnel) and wind tunnels across the United States to cover the Mach number and Reynolds number ranges of flight. The application of CFD in these efforts was used to support the wind tunnel testing through comparison with the measured data and by interrogating the solutions to better understand the fluid dynamics. CFD applications to the flight vehicle were also made to assess extrapolation of the wind tunnel data to flight conditions.

During the series of hypersonic tests, over 600 runs were made in the four LaRC aerothermodynamic facilities. Tests were performed for angles of attack from –4 to 50 deg and sideslip angles from –4 to 4 deg to measure the aerodynamic forces and moments. The effects of control surface deflections were studied by testing body flap settings between –15 and 30 deg and elevon settings between –30 to 30 deg. No rudder deflections were considered at the hypersonic conditions studied. By conducting tests in both Mach 6 and Mach 10 air flows a Mach number effect could be inferred in the aerodynamic database. Similarly, tests at Mach 6 in both air and CF_4 were used to simulate real gas effects through the variation in shock density ratio produced in the different test gases. Tests showed a measurable effect over the Reynolds number range in each facility, but the effect was quite small and is not discussed in this paper. Tests in Mach 20 helium were used for screening and rapid assessment with stereolithography (SLA) models and were not part of the aerodynamic database. CFD solutions using the LAURA and GASP Navier-Stokes codes and the FELISA Euler code were obtained [21,22] over the high angle of attack range for both Mach 6 air and CF_4 and Mach 10 air. Viscous solutions with deflected body flap controls were also modeled in the computations.

A complete review of the hypersonic aerodynamic characteristics established in the LaRC tests has been presented by Murphy, et al. [23]. In general, the tests showed the vehicle to have a linear lift curve for α<40 deg and a hypersonic L/D of approximately 1 at trim condition. A good comparison between measurement and computation of axial force (C_A) and normal force (C_N) was found across the angle of attack and Mach number range. The experiments showed the vehicle to be roll stable for α > 4 deg and to posses positive dihedral effect. Not surprisingly, the vehicle displayed directional instability for all angles of attack at these hypersonic conditions due to the high incidence and shadowing of the vertical tail surfaces. This is a common trait of a winged or lifting-body entry vehicle that is typically mitigated with reaction control jets.

4.1.1 Longitudinal Control

Hypersonic pitching moment (C_m) is presented in Figure 7 as a function of angle of attack for Mach 6 and 10 conditions in air. As shown in the figure, the vehicle exhibits longitudinal instability for $\alpha < 10°$, neutral stability for $10° < \alpha < 24°$, and then marginal stability for higher angles of attack. The measured data and the CFD predictions display a crossover of pitching moment between the Mach 6 and Mach 10 conditions where the crossover was measured to occur around $\alpha=30°$ but is predicted by CFD to occur around $\alpha=42°$. A parametric CFD study [21] confirmed a consistent trend of decreasing stability (and crossover) with decreasing Mach number for the X-33, and pitching moment data from other configurations (i.e. winged bodies and lifting bodies) tested in the LaRC Mach 6 and 10 air tunnels show similar Mach number effects. Subsequent configuration build-up studies on X-33 identified the fuselage alone as the source of the Mach number effect, although the exact cause has not been determined.
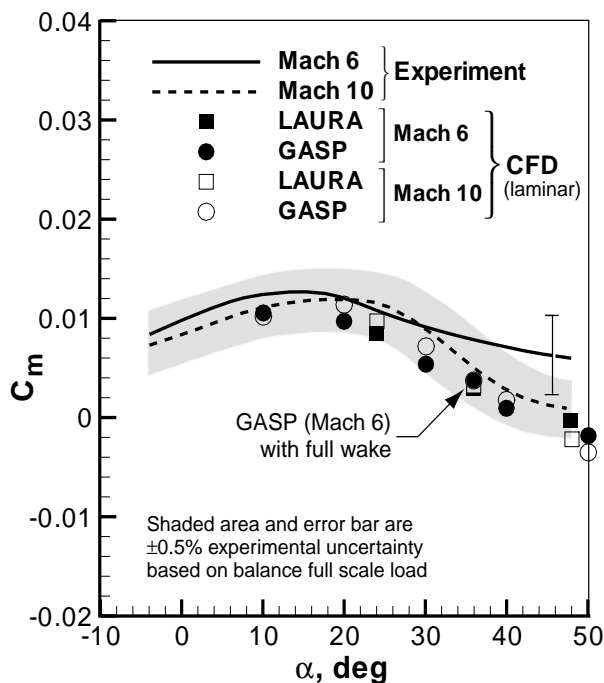
The largest disagreement between measured and predicted pitching moment occurs in the angle of attack range above $\alpha=30°$, particularly for Mach 6 where the prediction is outside the experimental uncertainty band. The discrepancy for Mach 6 naturally raised concerns with both the CFD predictions and wind tunnel measurements since the baseline vehicle (zero control deflections) was less stable with decreasing Mach number. It was thought that the failure to model the base and wake region in the computations could present some error; however, a CFD solution with the full laminar wake at $\alpha=36$ deg showed little effect of the base flow on the baseline pitching moment (Figure 7). Comparing results from the configuration build-up tests with the moments computed over individual components isolated the source of the disagreement to the fuselage alone.

One additional study was performed using a sparsely instrumented pressure model in a rapid attempt to understand the differences in the experimental and computational results for Mach 6 and 10 air. The pressure tests suggested that differences existed in the measured and predicted pressure on the wind side forebody in an area of overexpansion and recompression downstream of the nose cap. However, a consistent explanation for both Mach 6 and 10 could not be drawn and the results were inconclusive. A high fidelity, highly instrumented pressure model is required to provide the necessary information to explain the fluid dynamic phenomena causing the Mach number effect and resolve the disagreement between experiment and computation. Nevertheless, it is important to note that the discrepancies in pitching moment coefficient due to variation in Mach number from 6 to 10 are small (on the order of 0.008) and that the X-33 body flaps produce sufficient authority to control the vehicle as discussed in the next section.

Figure 7. Comparison of measured and predicted pitching moment (baseline). (adapted from Murphy, et al. [23]).

4.1.2 Control Surface Effectiveness

Rear-mounted body flaps (Figure 2) provide the primary pitch control on the X-33 vehicle during unpowered descent. The effectiveness of these flaps is illustrated in Figure 8, which shows the pitching moment curves for positive flap deflections (δ_{BF}) of 10 and 20 deg at Mach 10. Mach 6 measurements (not shown) are similar but slightly less stable and slightly under predicted by the CFD (as was observed for the baseline case).
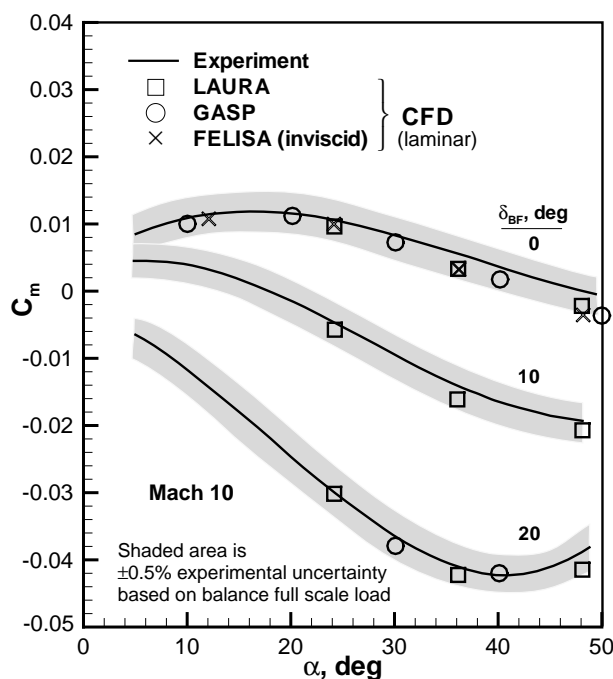
Figure 8. Comparison of measured and predicted pitching moment with deflected body flaps (from Hollis, et al. [4]).

From a programmatic viewpoint, the curves show that the vehicle has more than sufficient control authority for stability and trim and the previously discussed uncertainties in pitching moments translate to approximately 2-3 deg of body flap deflection. From a fluid dynamic perspective, the curves portray degradation in flap effectiveness as angle of attack and/or body flap deflection are increased. This degradation is due primarily to an interaction between the bow shock and deflected flap shock that produces a reflected expansion fan over the flap surface. The CFD predictions captured this interaction and the corresponding influence on aerodynamic characteristics very well, thereby complementing the experimental data and providing invaluable information toward understanding the structure of this complex flow field.
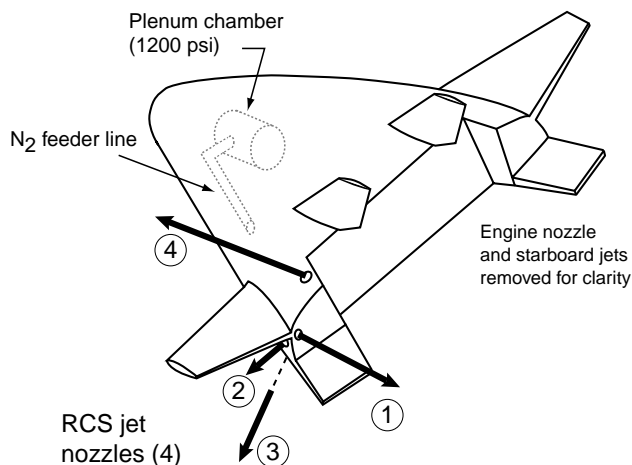
4.1.3 Reaction Control System (RCS)

Reaction control jets are an integral component of space transportation systems since they are required for on-orbit maneuver and provide control when aerodynamic forces are insufficient during periods of low-density flight or high vehicle incidence. In the case of X-33, the planned trajectory remains within the sensible atmosphere but includes high angle of attack bank maneuvers that require a RCS. A primary issue in RCS design is the possible aerodynamic influence of interactions produced between a firing jet plume, the surrounding flow field, and the vehicle surface. These RCS interactions are difficult to accurately predict at flight conditions and can be significant as was learned for the Shuttle Orbiter during the first flight (STS-1) [24].

A system of eight aft-end thrusters (4 per side) was designed for the X-33 vehicle to provide the needed pitch, yaw, and roll control as shown in Figure 9. A series of experimental tests was performed in the Mach 10 air and Mach 6 air tunnels and the LaRC UPWT at Mach 4 to determine the level of interaction effects on the X-33 aerodynamics. Tests were performed with a 1% scale model and unheated, high-pressure nitrogen gas was used to simulate the thruster's jet plumes. Chamber pressure to the thruster nozzles was varied from 400 to 1200 psi to simulate the change in jet plume shape with altitude during flight. Three sets of conical nozzles with exit half-angles between 10 and 30 deg were tested to simulate the change in plume shape during flight due to the different specific heat ratios (γ) in the actual jet and external flow field. Variation of these simulation parameters was guided by Shuttle flight data where Scallion [25] showed matching momentum ratio of the jet and freestream gave the best correlation between wind tunnel data and flight. RCS interaction on deflected control surfaces (body flap, elevon, and rudder) was also examined during the experiment. Results from these tests provided the vehicle designers with a complete set

of force and moment increments on the baseline aerodynamics that could be used to evaluate interaction effects and design control systems. It was found that side-firing jets located below the X-33 canted fins (jet nozzle number 2 in Figure 9) produced uncontrollable rolling moments due to interactions with the fin and these yaw-control jets were subsequently moved to the vehicle base.

Figure 9. Sketch of wind tunnel model for reaction control system (RCS) tests.

4.2 Aerothermodynamics

The contributions to the aerothermodynamic design for X-33 summarized in this paper include continued development and validation of the tools used to predict the aeroheating environment and the application of these tools for design and benchmark data. Development of aerothermodynamic tools progressed on two fronts. Firstly, use of thermographic phosphors for heating measurements eliminated the usual situation where experimental aerothermodynamic analysis lags the aerodynamic analysis due to the complexity of aerothermodynamic models and instrumentation. The use of ceramic phosphor models provided an opportunity to conduct both type of analyses in parallel. This is an important step since aerodynamic optimizations often change the outer mold line shape that in turn requires more aeroheating assessment. The second area of development pertained to the prediction of hypersonic boundary layer transition on X-33. Although progress

has been made in predicting transition from theory, in practice vehicle designers still rely on semi-empirical techniques such as used for Shuttle. However, advances in CFD tools and global experimental techniques (e.g. thermographic phosphors) have significantly improved these techniques both in accuracy and in time required for analysis.

Over 1100 runs were performed in the LaRC AFC during the coarse of this work to provide essentially all of the experimental aeroheating data for the X-33 program. Tests were performed [26,27] in the Mach 6 air facility at angles of attack from –5 to 40 deg to simulate both ascent and descent conditions. Body flap deflections between 0 and 20 deg were studied and freestream Reynolds numbers based on body length were varied from 0.8 to 6.6 million in the facility. Thermographic phosphor measurements were used to capture heating distributions for the vehicle acreage as well as for specialized areas of heating. The following sections describe the results of these global and local aeroheating studies including the supporting computations.

4.2.1 Global Aeroheating

Aeroheating analyses were performed [28] during X-33 Phase I using a limited number of CFD solutions at points along the flight trajectory coupled with approximate methods to populate an aeroheating database. A similar method was employed [29] in Phase II to refine the aeroheating LMSW X-33 database. Validation of the CFD codes used to anchor the databases (i.e. LATCH and GASP) was accomplished by comparison of computed heating rates to those measured in the hypersonic wind tunnel tests. Additional comparison of results from the different computational tools (i.e. code-to-code comparisons) at both wind tunnel and flight conditions added confidence to the predictions in both environments. Ultimately, comparison of predicted results (whether experimental or computational) with measured flight data will provide the final verification. Prior to obtaining such flight-test data for the X-33, comparisons with existing flight data (e.g.

Shuttle orbiter) is used as documented for the LAURA code in [30-32].

Figure 10 illustrates a typical comparison between experimental and computational heating rate along the X-33 windward centerline. In this case, both laminar and turbulent GASP solutions are compared with thermographic phosphor data at Mach 6 for various values of Reynolds number. The data exhibit a transitional behavior beginning at the aft end and moving forward as Reynolds number is increased. The computed heating rates are shown to agree well with the laminar experimental data and with the turbulent data obtained by tripping the flow.
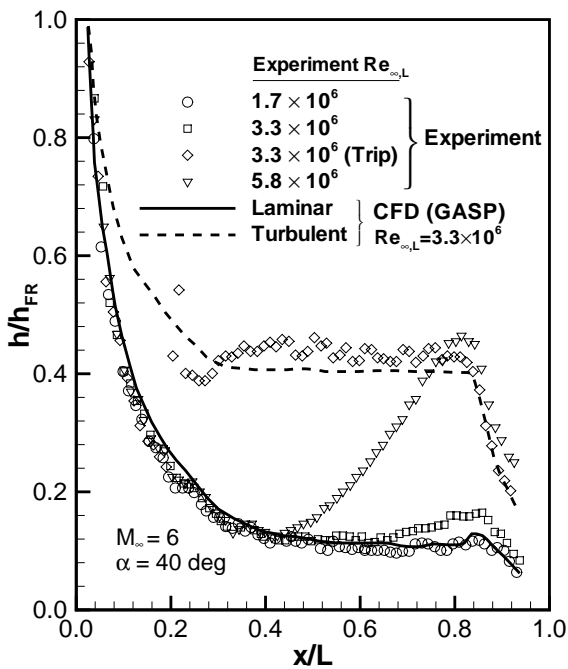

Figure 10. Comparison of measured and predicted heating along windward centerline (from Hollis, et al. [4]).

Figure 11 compares measured lateral distributions of windward heating data with predictions using the GASP and LATCH codes at two axial locations. Agreement is good with the exception that LATCH over predicted heating in the centerline region as shown in Figure 11(a). LATCH predictions in this region compared better with GASP predictions and measurement as angle of attack was increased. For the most rearward axial station (Figure 11(b)), the predictions and experimental data are in reasonably

good agreement across the span. Note that the lateral distribution at this location includes both the windward fuselage and the canted fin surfaces. LATCH does a remarkable job capturing this complex heating pattern.
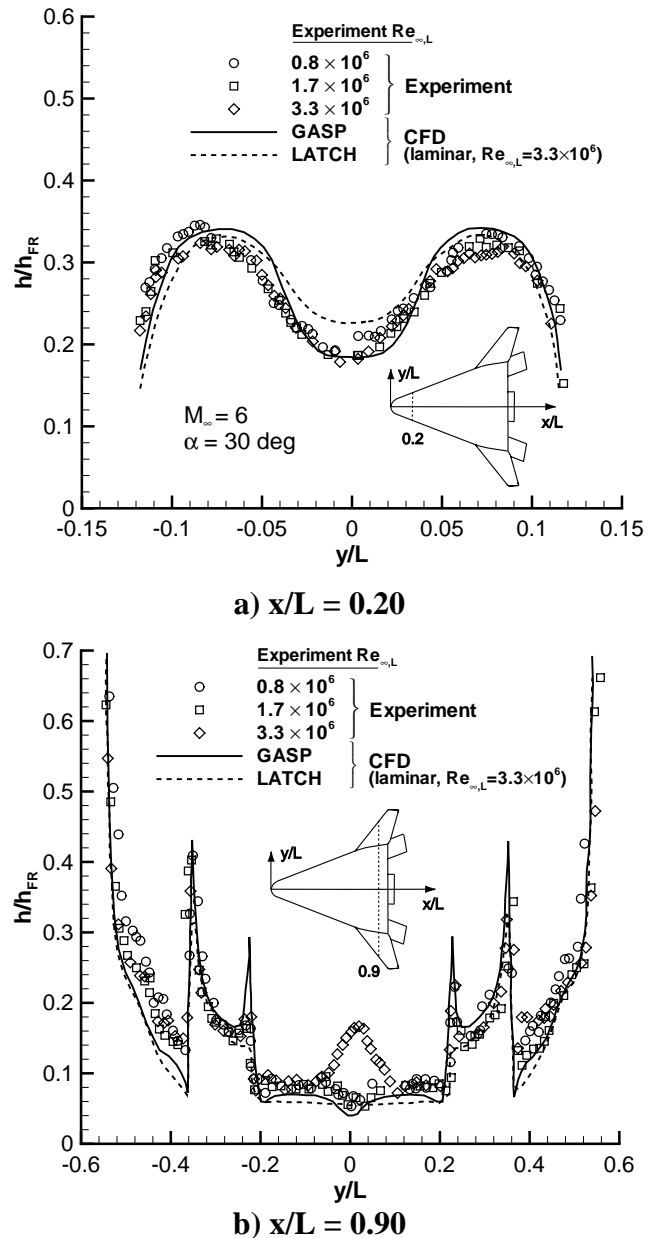

a) x/L = 0.20

b) x/L = 0.90

Figure 11. Comparison of measured and predicted heating along lateral windward lines (from Hollis, et al. [21])

In other comparisons, it was found that laminar CFD computations generally predicted the leeside measured heating rate within experimental uncertainty. Finally, a typical comparison between computations via the GASP

and LAURA codes at flight conditions is shown in Figure 12 where contours of radiation equilibrium temperatures show excellent agreement. (The reader is referred to [33,21,4] for additional examples of data and code-to-code comparisons).
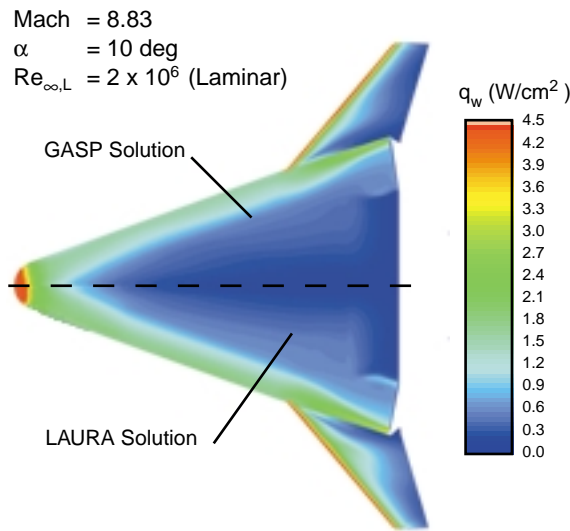

Mach = 8.83
α = 10 deg
$Re_{\infty,L}$ = 2 x 10^6 (Laminar)

GASP Solution

LAURA Solution

q_w (W/cm^2)

Figure 12. Comparison of predicted heating for flight (from Hollis, et al. [21]).

A successful effort to extrapolate thermographic phosphor heating measurements directly from the wind tunnel (i.e. immediately following a tunnel run) to a full-scale vehicle at flight conditions was demonstrated for the X-34 [10,34]. At present, this technique is capable of providing radiation equilibrium wall temperatures in flight for perfect gas, laminar or turbulent flows as part of the wind tunnel data reduction process. An example of this technique applied to X-33 is presented in Figure 13 for a 40-deg angle of attack condition. Here a Mach 6 wind tunnel measurement at length Reynolds number of $Re_{\infty,L}=2\times10^6$ was extrapolated to a flight environment at Mach 6.6, $Re_{\infty,L}=5\times10^6$, and 146730 ft (44.7 km) altitude. The figure compares the surface temperatures extrapolated along the windward centerline with predicted results from GASP at the flight condition. Temperatures from the two predictions are generally within 50 ºF. Obtaining such information during the rapid, global aeroheating tests afforded by the phosphor technique is extremely useful to vehicle designers. Work to further validate and extend the extrapolation procedure

to real gas flows is ongoing with the goal to develop a rapid technique for TPS material selection, split line definition, and material sizing.
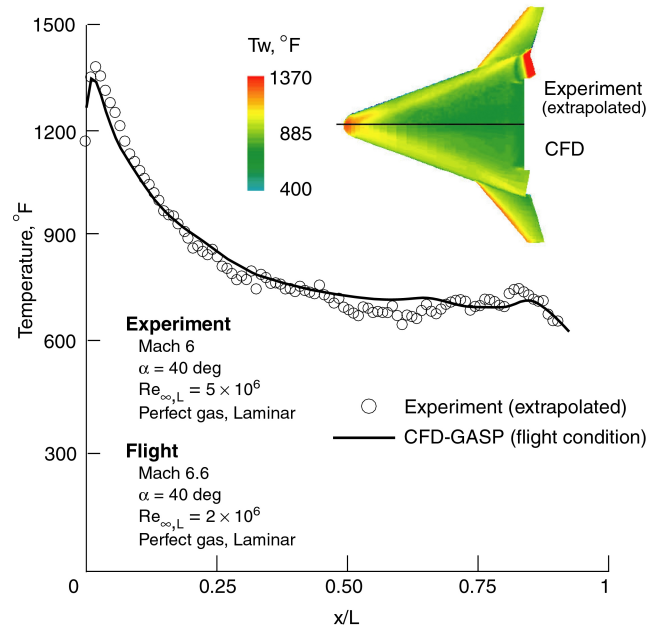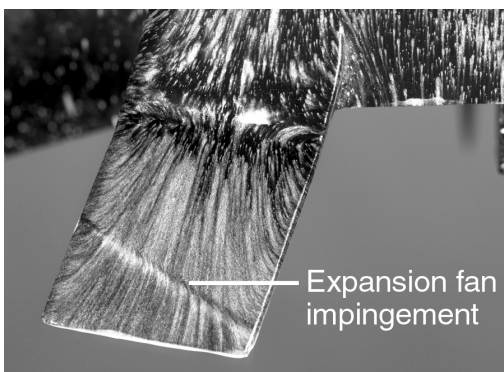

Figure 13. Extrapolation of laminar experimental heating data to flight condition (from Horvath, et al. [26]).

4.2.2 Local Aeroheating

Three areas of prominent heating on X-33 warranted detailed investigation; the deflected body flap surfaces, the canted fin surface and leading edge, and the aerospike nozzle. Results of those investigations [26,28] are briefly summarized here. Horvath, et al. [26] used phosphor thermography, schlieren images, and oil flow patterns to investigate the flow separation and reattachment around the body-flap hinge line and the interaction effects on body flaps with 10 and 20-deg deflections. Ratios of deflected to undeflected flap heating were derived for use in estimating heating augmentation over the undeflected level. The augmentation at angles of attack between 30 and 40 deg was found to increase linearly with deflection angle, with maximum values of 5 to 7 over a laminar undeflected reference and 2 to 3 over a turbulent reference. The augmentation factors were found insensitive to the state of the approaching boundary layer (laminar or turbulent), which suggests that the flow was transitional, if not fully turbulent, over the deflected surfaces.

Separation in
front of flap

Heating at flow
reattachment

Heating at expansion
fan impingement

h/h_{FR}
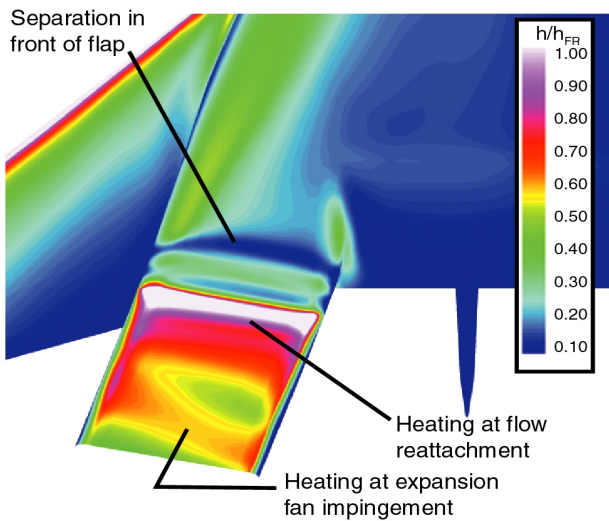
a) **Computed heating contours, $Re_{\infty,L} = 3.3 \times 10^6$ (from Hollis, et al. *[4]*)**

Expansion fan
impingement

b) **Oil flow image, $Re_{\infty,L} = 1.7 \times 10^6$ (from Horvath, et al. *[26]*)**

Figure 14. Shock interaction effects on deflected body flap, $M_\infty = 6$, $\alpha = 40$ deg.

The outboard location of the X-33 body flaps results in the deflected flap shock being in close proximity to the windward bow shock. The interaction of these shocks produces a reflected expansion fan that was shown (Figure 8) to cause degradation of the flap aerodynamic effectiveness. It is not surprising that the interaction adversely affects the aerodynamic heating over the flap surface as well. Inspection of the phosphor temperature images reveals a local heating peak produced by a thinning boundary layer where the expansion fan impacts the sur-

face. Solutions obtained with the GASP code (Figure 14(a)) depict this local peak heating in addition to the separation and reattachment around the hinge line. These predicted heating contours were in qualitative agreement with the phosphor images although the experiment suggested the flow downstream of reattachment was transitional/turbulent and calculations assumed a laminar flow. Oil flow images such as shown in Figure 14(b) clearly reveal the effects of body flap impingement and show good correlation with the heating contours. (The interaction effect on the body flaps was not observed in studies on earlier X-33 configurations with shorter length flaps).

A second area of shock interaction exists on X-33 between the bow shock and the shock formed on the leading edge of the canted fin. Horvath, et al. [26] found that this interaction occurred at all angles of attack tested and most closely resembled a Type VI. Although heating to the fin leading edge in the region of the shock interaction could not be discerned from the phosphor measurements, the global images over the fin surface did offer useful information. At low angles of attack, the shock interaction produced local elevated heating rates on the upper fin surfaces due to the negative incidence of the fin. This region of elevated heating moved to the lower fin surface with increasing angle of attack but the corresponding level was also diminished. The disturbed flow downstream of the shock interaction was sensitive to Reynolds number as expected, with transition over the fin surface observed for $Re_{\infty,L} > 3.3 \times 10^6$ at all angles of attack.

The aerospike engine nozzles on X-33 extend well into the wake flowfield (see Figure 2) and are unshielded from impingement of separated flow off the windward fuselage. An assessment of aeroheating to the nozzles and base was critical given the high incidence angles during descent and both experimental [26] and computational studies [28] were undertaken for this purpose. Data from thermographic phosphor measurements indicated that heating rates on the nozzle reached 10% of the nose stagnation heating in the area of impingement. In comparison, calculations at the flight peak

heating point using the LAURA code predicted heating rates on the order of 5% of the nose stagnation value using a radiation equilibrium wall temperature and a surface emissivity of 0.15 on the nozzle. The complexity of the CFD analysis needed to obtain these results is illustrated in Figure 15 which shows that 250 Cray C-90 hours were required to obtain a solution and that 65% of the total time was required to resolve the wake. This was a critical calculation that led to the design of a system that circulates hydrogen fuel through the structure during descent to actively cool the nozzle.
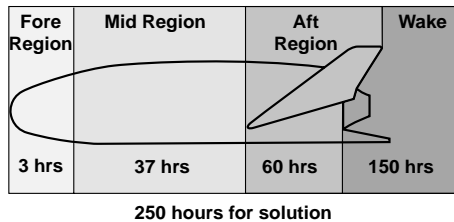
a) Computer resources required
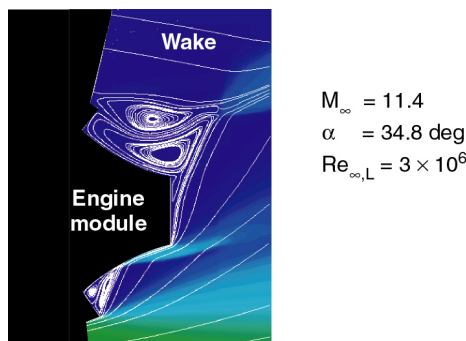
**b) Computed streamlines and pressure contours**

Figure 15. Computation of wake flow and impingement on aerospike nozzle (from Miller *[6]*).
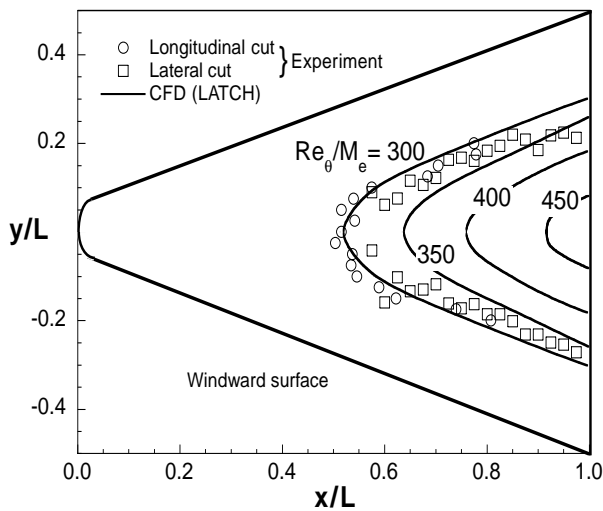
4.2.3 Boundary Layer Transition

A majority of the aerothermodynamic wind tunnel testing performed for X-33 and a significant computational effort was directed toward understanding and developing a correlation for hypersonic boundary layer transition on the windward fuselage. The steps taken to investigate wind side transition were straightforward but the order in which the results were applied was somewhat reversed due to the fast-paced nature of the program. To explain further, the vehicle designers used a "worst case" aeroheating tra-

jectory to design the TPS prior to finalizing the transition correlation by assuming that turbulence would occur below a certain point during descent. Once a correlation was developed, then the original assumption regarding transition onset would be revised, if necessary, and any roughness constraints applied. It was assumed in the program that the flow adjacent to the lee-side and body flap surfaces would always be turbulent while the flow over the canted fin would transition 30 seconds prior to the flow over the fuselage. As a result, the work reviewed in this section focused exclusively on fuselage transition.

The first step in developing a transition criterion was to perform thermographic phosphor tests on a smooth model in the 20-Inch Mach 6 tunnel over a range of Reynolds numbers and attitudes and attempt to correlate the transition fronts with the parameter Re_θ/M_e. Here, Re_θ is the momentum thickness Reynolds number and M_e the boundary layer edge Mach number, both of which were extracted from LATCH solutions. As an example, Figure 16(a) presents a phosphor image of the transition front on the windward fuselage at 40-deg angle of attack while Figure 16(b) shows a correlation of this front for a value of $Re_\theta/M_e = 300$. Applying this process to all test conditions yielded values between 250 and 325 and an average value of $Re_\theta/M_e = 285$ was chosen to represent the whole dataset thereby giving a constant "smooth body" ratio.
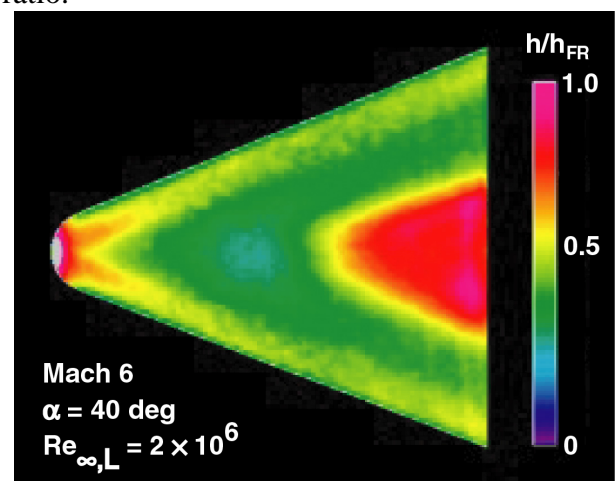


a) Thermographic phosphor image

b) Correlation with Re_θ/M_e parameter

Figure 16. Correlation of boundary layer transition on "smooth" forebody (from Thompson, et al. [35]).

The smooth-body transition tests provided an upper bound on the Re_θ/M_e parameter since transition would occur at lower values if roughness effects promoted transition. Using calculations at flight conditions corresponding to the trajectory point where transition was assumed during the TPS design it was found that a value of $Re_\theta/M_e = 250$ corresponded to a location on the windward centerline at 80% of the length. This value was ultimately adopted as the X-33 transition criterion. To insure that transition due to roughness would not occur earlier in the trajectory, a correlation between Re_θ/M_e and roughness height was needed to determine a maximum allowable roughness for the vehicle.
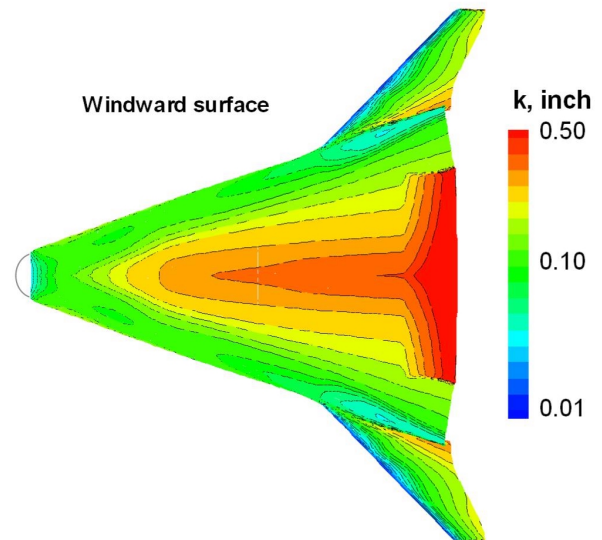
Berry, et al. [36] developed a successful correlation of wind-tunnel data for discrete roughness elements on the Shuttle Orbiter that related Re_θ/M_e with k/δ, where k is the roughness height and δ is the boundary layer thickness. A similar approach was used to obtain a correlation for X-33 whereby raised square patches of varying thickness were applied at discrete surface locations and the phosphor thermography technique used to determine the "incipient" and "effective" transition Reynolds number. An "incipient" value corresponded to the highest Reynolds number that maintained laminar flow downstream of the trip while an "effective" value corresponded to the minimum Reynolds number where the transition front was fixed at the roughness element. Tunnel conditions were varied for a given roughness height, trip location, and angle of attack to locate these incipient and effective Reynolds numbers. Roughness elements were fabricated from 0.0025-inch Kapton tape which could be stacked in multiple layers to provide thickness variation. The elements simulated the effect of a raised TPS panel and were oriented with the diagonal aligned to the local flow, much like the herringbone pattern of the metallic TPS. Roughness elements were tested at six locations along the windward centerline and at four locations along the attachment line. Attachment lines on X-33 are confined outboard near the fuselage chines for the angles of attack studied (20, 30, and 40-deg) and location of the lines was determined via oil flow images and computational predictions prior to the subject tests. With this arrangement, a systematic testing of roughness height, location, and angle of attack was performed and the incipient and effective transition Reynolds numbers determined. Computing Re_θ/M_e and boundary layer thickness at each trip location for all effective and incipient pairs provided the necessary information to establish a correlation between roughness and transition. Figure 17 shows the resulting data and displays a generally well-behaved trend in terms of Re_θ/M_e vs. k/δ. The lines in the figure represent "conservative" curve fits of the data that delineate a region of laminar flow below the dashed line (the "incipient" curve) and a region of turbulent flow above the solid line (the "effective" curve).
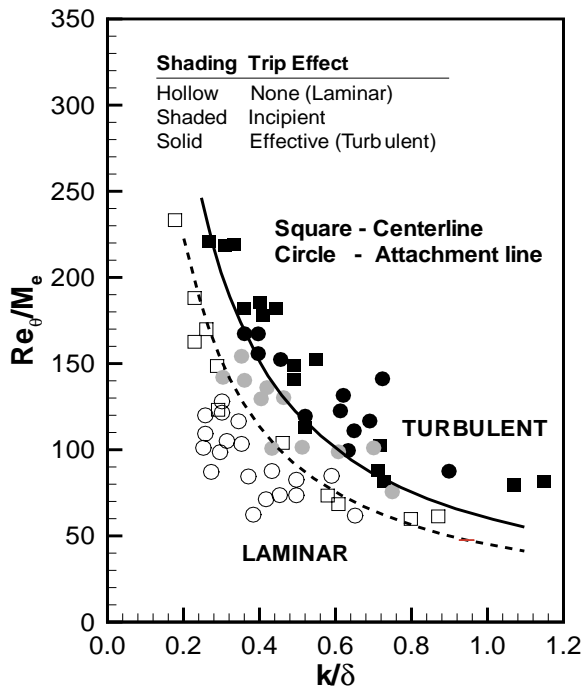
Figure 17. Experimental correlation of X-33 transition with roughness from discrete trips (from Berry, et al. *[37]*).

Figure 18. Maximum allowable roughness on full-scale vehicle based on experimental correlation of X-33 transition (from Thompson, et al. *[35]*).

The incipient curve shown in Figure 17 provided a basis for determining allowable roughness heights on the X-33. Using this figure with the value of Re_θ/M_e =250 (as determined for X-33) gives $k/\delta \cong 0.2$. Applying this constraint ($k/\delta \cong 0.2$) to the surface boundary layers calculated at the transition trajectory point used in the TPS design yielded the allowable heights over the vehicle shown in Figure 18. Roughness height less than the allowable should be negligible while larger values would cause transition earlier than anticipated. Comparison of the allowable heights to the manufacturing tolerances on X-33 revealed that the roughness constraints were easily met (except possibly near the fin root).

Another transition issue investigated for X-33 was the effect of a distributed roughness caused by bowing of the metallic TPS panels expected in flight. This bowing is specific to X-33 due to a rapid heat pulse associated with the sub-orbital flight trajectory; bowing would not be expected on an RLV during reentry from LEO. Figure 19 illustrates five configurations of bowed panel arrangements that were tested. Three different bow heights were tested (0.002, 0.004, and 0.008 inch) with the two smallest values being geometrically scaled from the expected bowing for the full-scale vehicle. The wavy surface introduced clear flow field perturbations observed in oil flow and schlieren images, particularly for the largest two bow heights. However, it was found that all of the configurations with bow heights smaller than the maximum value were less effective at producing transition than the discrete roughness elements. It was concluded [37] that the bowed wall did not cause any additional sensitivity to roughness beyond the correlation already developed using discrete roughness elements.
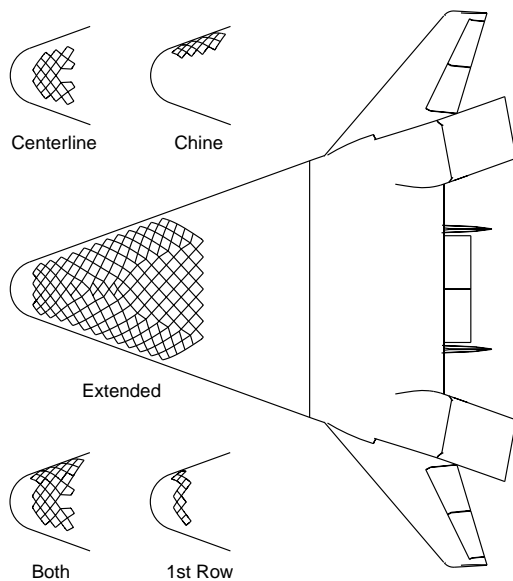
Figure 19. Configurations tested for bowed panel roughness test (from Berry, et al. [37]).

The simple Re_θ/M_e criterion developed for X-33 enabled construction [35] of a semi-analytic model to predict whether transition occurs at a station on the windward centerline for a given altitude, velocity, and angle-of-attack condition. This model is based on a database of numerical simulations that cover the range of freestream and angle of attack values expected during flight. For X-33, a domain in trajectory space was selected where altitude ranged from 30 to 80 km for freestream velocities between 1 and 5 km/s and angles of attack between 0 and 40 deg. A total of 275 flow solutions were computed for discrete combinations of these parameters. Each calculation was performed using the LATCH code to provide a distribution of Re_θ/M_e along the windward centerline. Since LATCH requires edge properties from an inviscid flowfield solution, it was necessary to make an approximation for the approach to be practical by using a single inviscid solution at each angle of attack for all altitudes and velocities. This approximation is valid for all altitudes (except when real gas effects are important) since the inviscid solution is independent of Reynolds number. It is valid for velocities where the Mach number is large (M>8) since the shock shape and normalized pressure distributions are nearly invariant. To improve the accuracy of inviscid edge properties for the X-33 trajectory,

inviscid equilibrium air solutions were obtained for Mach 10 cases at angles of attack between 20- and 40-deg and Mach 6 perfect gas solutions were used for angles between 0 and 15 deg.

A relationship for transition at a body point was derived by interpolation of the LATCH database to locate the altitudes where transition occurs for all combinations of velocity and angle of attack. Figure 20 shows this relationship using the X-33 criterion ($Re_\theta/M_e=250$) and a point at x/L=0.8 on the windward centerline. The result is a nearly planar surface in three-dimensional trajectory space that separates laminar flow above from turbulent flow below. In practice, this function can be used to identify regions of transition by plotting a trajectory in this space and locating the point where the path intersects the surface as shown in the figure. In addition, the sensitivity of transition onset to the value of Re_θ/M_e and the movement of transition along the vehicle can be studied by varying the parameters used for interpolation in the database. A computer routine to evaluate the transition model for X-33 was developed that provided invaluable information to the vehicle designers leading to tailoring of trajectories in order to remain within TPS design limits.
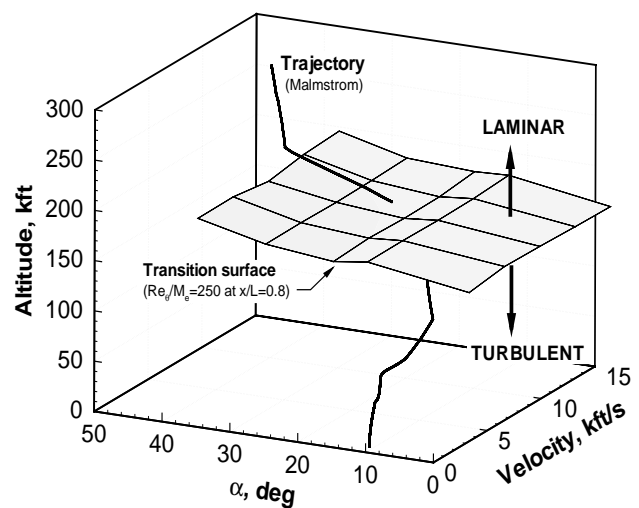
Figure 20. Transition criterion in trajectory space (from Thompson, et al. [35]).

5 Summary

Development of a sub-scale flight vehicle (X-33) to demonstrate technologies for a new reusable launch system in the United States has ensued over the past five years. The new technologies and the rapid program pace have presented many challenges to industry and government teams. In this paper, an overview of several major studies conducted by the Aerothermodynamics Branch at NASA LaRC to support development of the LMSW X-33 vehicle is presented. These studies provided aerodynamic and aeroheating screening, optimization, and benchmarking of the X-33 and utilized the unique capabilities offered by the LaRC Aerothermodynamics Facilities Complex coupled with the application of computational tools (both detailed CFD and engineering level).

Extensive wind tunnel testing in the LaRC Mach 6 and 10 air tunnels and Mach 6 CF_4 tunnel contributed significantly to the establishment of the flight databook for the hypersonic longitudinal and lateral aerodynamic characteristics, control surface effectiveness, and reaction control system effects. Measurements from these tests showed the baseline vehicle (zero control deflections) to be marginally stable in longitudinal pitch and laterally unstable at the high trim angles of attack (45 to 50 deg). Measurement and prediction revealed the vehicle became less stable as Mach number decreased from 10 to 6 and the source of this trend was isolated to the vehicle fuselage. While this Mach number effect was qualitatively predicted by computation and the measured and predicted pitching moment were in good agreement at Mach 10, the prediction at Mach 6 fell outside the experimental uncertainty.

Wind tunnel tests with deflected body flap surfaces showed the vehicle to have more than sufficient authority for pitch control, which mitigated concerns about the decreasing stability with Mach number. Body flap effectiveness suffered degradation with increasing deflection angle and increasing angle of attack due to a shock interaction and impingent of a reflected expansion fan on the flap surface. Predictions

with CFD codes significantly enhanced the understanding of the complex flowfield around the deflected flap and were in good comparison with the measured pitching moments. Extensive wind tunnel testing on an X-33 model with reaction control jets was performed to establish a database for the aerodynamic effect of jet interaction with the flowfield and vehicle surface. Side firing jets were moved to the base region as a result of these tests.

Global heat transfer distributions measured using a thermographic phosphor technique in the Mach 6 air tunnel were in good agreement with predictions from the CFD codes used to define the aerothermal environment in flight. Detailed studies of the aerodynamic heating to the deflected flap surfaces, aerospike engine nozzle, and fin leading edge were performed with the phosphor technique to provide information about these critical regions to the vehicle designers. Predicted engine nozzle heating due to an impingement from the wind-side flow field at flight conditions compared reasonably well with wind tunnel measurements. These values of predicted heating and temperatures in flight contributed significantly to the decision to employ active cooling to the engine nozzles using hydrogen fuel during unpowered descent.

Global aeroheating tests at Mach 6 over a range of Reynolds number and incidence for a "smooth body" with and without discrete roughness trips along the windward centerline and outboard attachment lines were correlated to give a relation between the boundary layer transition parameter (Re_θ/M_e) and the roughness height. Applying this roughness correlation at flight conditions produced a surface map of the maximum allowable roughness heights for the full-scale vehicle. Fabrication and testing of thermographic phosphor models with "wavy-wall" surfaces to simulate bowing of metallic thermal protection tiles in flight was performed. These tests revealed that the discrete trips were more efficient generators of boundary layer transition than the wavy wall. The transition parameter established in the experimental work was used to derive a semi-analytic model capable of predicting transition for X-33 at points on the windward fuselage over a wide range of al-

titude, velocity, and angle of attack. Vehicle designers used this model to tailor trajectories so not to exceed the TPS design limits.

This review of studies performed at NASA LaRC to support the full breadth of hypersonic aerodynamic and aerothermodynamic issues for X-33 demonstrates the advantages and credibility afforded by synergism between experimental and computational capabilities. The ability to analyze critical aerodynamic and aerothermodynamic design issues is greatly enhanced by the synthesis of these disciplines.

6   Acknowledgement

The studies reviewed in this paper are the product of many months of outstanding and time-critical effort by many people. The author would like to credit all those who did the work cited in the text and express thanks for assistance in compiling this paper. Equal gratitude is extended to the many others who supported these efforts in every other way.

References

[1]   Bekey I, Powell R and Austin R. NASA Studies Access to Space. In *Aerospace America*, 1994; pp 38-43.

[2]   Lockwood M K. Overview of Conceptual Design of Early VentureStar Configurations. AIAA 2000-1042, 2000.

[3]   Reed R D. The Lifting Body Story. NASA SP-4220, 1997.

[4]   Hollis B R, Horvath T J, Berry S A, Hamilton H H, II and Alter S J. X-33 Computational Aeroheating Predictions and Comparisons With Experimental Data. AIAA 99-3559, 1999.

[5]   Miller C G. Development of X-33/X-34 Aerothermodynamic Data Bases: Lessons Learned and Future Enhancements. *NATO-AVT Symposium on Aerodynamic Design and Optimization of Flight Vehicles in a Concurrent Multi-Disciplinary Environment*, Ottawa, Canada, 1999.

[6]   Miller C G. Aerothermodynamic Flight Simulation Capabilities for Aerospace Vehicles. AIAA 98-2600, 1998.

[7]   Micol J R. Langley Aerothermodynamics Facilities Complex: Enhancements and Testing Capabilities. AIAA 98-0147, 1998.

[8]   Buck G M. Automated Thermal Mapping Techniques Using Chromatic Image Analysis. NASA TM 101554, 1989.

[9]   Buck G M. Surface Temperature/Heat Transfer Measurement Using a Quantitative Phosphor Thermography System. AIAA Paper 91-0064, 1991.

[10]   Merski N R. Global Aeroheating Wind-Tunnel Measurements Using Improved Two-Color Phosphor Thermography Method. *Journal of Spacecraft and Rockets*, Vol. 36, No. 2, pp 160-170, 1999.

[11]   Buck G M and Vasquez P. An Investment Ceramic Slip-Casting Technique for Net-Form, Precision, Detailed Casting of Ceramic Models. U.S. Patent 5,266,252, 1993.

[12]   Hamilton H H, II, Greene F A and DeJarnette F R. Approximate Method for Calculating Heating Rates on Three-Dimensional Vehicles. *Journal of Spacecraft and Rockets*, Vol. 31, No. 3, pp 345-354, 1994.

[13]   Zoby E V, Moss J N and Sutton K. Approximate Convective Heating Analysis for Hypersonic Flows. *Journal of Spacecraft and Rockets*, Vol. 18, No. 1, pp 64-70, 1981.

[14]   Peiro J, Peraire J and Morgan K. FELISA System Reference Manual and User's Guide. NASA CP-3291, 1995.

[15]   Bibb K L, Periare J and Riley C J. Hypersonic Flow Computation on Unstructured Meshes. AIAA 97-0625, 1997.

[16]   Gnoffo P A. An Upwind-Biased, Point-Implicit Algorithm for Viscous, Compressible Perfect Gas Flows. NASA TP 2953, 1990.

[17]   Aerosoft. GASP Version 3 User's Manual. Aerosoft, Inc., Blacksburg, VA, 1996.

[18]   Alter S J. Complex Volume Grid Generation Through the Use of Grid Reusability. AIAA 97-1987, 1997.

[19]   Alter S J. Solving Difficult Grid Related Problems Utilizing the Volume Grid Manipulator. 7th International Meshing Roundtable, Dearborn, MI, 1998.

[20]   Alter S J. Grid Generation Techniques Utilizing the Volume Grid Manipulator. AIAA 98-3012, 1998.

[21]   Hollis B R, Thompson R A, Murphy K J, Nowak R J, Riley C J, Wood W A, Alter S J and Prabhu R K. X-33 Aerodynamic and Aeroheating Computations for Wind Tunnel and Flight Conditions. AIAA 99-4163, 1999.

[22]   Prabhu R K. An Inviscid Computational Study of an X-33 Configuration at Hypersonic Speeds. NASA/CR-1999-209366, 1999.

[23]   Murphy K J, Nowak R J, Thompson R A, Hollis B R and Prabhu R K. X-33 Hypersonic Aerodynamic Characteristics. AIAA 99-4162, 1999.

[24]   Stone J S, Baumbach J J and Roberts B B. Space Shuttle Orbiter Reaction Control Subsystem Flight Data Anomalies. Shuttle Performance: Lessons Learned, Vol. 1, NASA CP-2283, pp 381-395, 1983.

[25]   Scallion W I. Space Shuttle Reaction Control System - Flow Field Interactions During Entry. Orbiter Experiments (OEX) Aerothermodynamics Symposium, Williamsburg, VA, Vol. 1, NASA CP-3248, pp 345-370, 1995.

[26] Horvath T J, Berry S A, Hollis B R, Liechty D S, Hamilton I, H. Harris and Merski N R. X-33 Experimental Aeroheating at Mach 6 Using Phosphur Thermography. AIAA 99-3558, 1999.

[27] Berry S A, Horvath T J, Kowalkowski M K and Liechty D S. X-33 (Rev-F) Aeroheating Results of Test 6770 in NASA Langley 20-Inch Mach 6 Air Tunnel. NASA/TM-1999-209122, 1999.

[28] Gnoffo P A, Weilmuenster K J, Hamilton H H, II, Olynick D R and Venkatapathy E. Computational Aerothermodynamic Design Issues for Hypersonic Vehicles. *Journal of Spacecraft and Rockets*, Vol. 36, No. 1, pp 21-43, 1999.

[29] Henline W and Bowles J. Development of an Aerothermodynamic Environments Database for Integrated Design of the Prototype Flight Tests Vehicle. AIAA 98-0870, 1998.

[30] Gnoffo P A. Code Calibration Program in Support of the Aeroassist Flight Experiment. *Journal of Spacecraft and Rockets*, Vol. 27, No. 2, pp 131-142, 1990.

[31] Gnoffo P A, Weilmuenster K J and Alter S J. Multiblock Analysis for Shuttle Orbiter Re-Entry Heating from Mach 24 to Mach 12. *Journal of Spacecraft and Rockets*, Vol. 31, No. 3, pp 367-377, 1994.

[32] Weilmuenster K J, Gnoffo P A and Greene F A. Navier-Stokes Simulations of Orbiter Aerodynamic Characteristics Including Pitch Trim and Bodyflap. *Journal of Spacecraft and Rockets*, Vol. 31, No. 3, pp 355-366, 1994.

[33] Hamilton H H, II, Weilmuenster K J, Horvath T J and Berry S A. Computational/Experimental Aeroheating Predictions for X-33 Phase II Vehicle. AIAA 98-0869, 1998.

[34] Berry S A, Horvath T J, Difulvio M, Glass C and Merski N R. X-34 Experimental Aeroheating at Mach 6 and 10. *Journal of Spacecraft and Rockets*, Vol. 36, No. 2, pp 171-178, 1998.

[35] Thompson R A, Hamilton H H, II , Berry S A, Horvath T J and Nowak R J. Hypersonic Boundary Layer Transition for the X-33 Phase II Vehicle. AIAA 98-0867, 1998.

[36] Berry S A, Bouslog S A, Brauckmann G J and Caram J M. Boundary Layer Transition Due to Isolated Roughness: Shuttle Results from the LaRC 20-Inch Mach 6 Tunnel. AIAA 97-0273, 1997.

[37] Berry S A, Horvath T J, Hollis B R, Thompson R A and Hamilton H H, II. X-33 Hypersonic Boundary Layer Transition. AIAA 99-3560, 1999.